Comparing Roles of Fault Friction and Upper-Plate Rigidity in Depth-Dependent Rupture Characteristics of Megathrust Earthquakes

Szu-Ting Kuo[1], Benchun Duan[1], and Qingjun Meng[1]

[1]Center for Tectonophysics, Department of Geology and Geophysics, Texas A&M University, College Station, TX 77840-3115, USA

Corresponding author: Benchun Duan (bduan@tamu.edu)

Key Points:

- Updip transition of velocity-dependent friction behavior near the trench suppresses rupture propagation toward the trench
- Depth-varying fault friction dominates high-frequency depletion at shallow depth
- Upper-plate low rigidity layers at shallow depth mainly enhance slip near the trench

Abstract

Megathrust earthquakes with a wide along-dip rupture extent show clearly depth-dependent variations in rupture characteristics such as rupture velocity, frequency contents of seismic radiation and slip distribution. Some recent studies propose that heterogeneous upper-plate rigidity determines this phenomenon, though along-dip variations in fault friction have long been thought to play a dominant role. In this study, we use dynamic rupture modeling to explore and compare roles of these two factors in depth-dependent rupture characteristics of megathrust earthquakes along a shallow-dipping subduction plane that is governed by the rate- and state-dependent friction. We find that an updip transition from velocity-weakening behavior downdip to velocity-strengthening behavior near the trench suppresses rupture propagation toward the trench and a thicker transition zone results in a more confined slip at depth. The updip transition in velocity-dependent frictional property also dominates high-frequency depletion in seismic radiation at shallow depth. With an addition of a conditionally stable zone at shallow depth, rupture velocity significantly decreases, resulting in longer rupture duration as the thickness of the conditionally stable zone increases. The low-velocity layers in the upper plate at shallow depth lead to a more compliant prism and thus significantly higher total slip near the trench. Although they place some limits to rupture velocity at shallow depth, they enhance high-frequency radiation and thus do not contribute to high-frequency depletion observed in recent megathrust earthquakes. We conclude that fault friction plays more important roles than upper-plate rigidity in determining depth-dependent rupture characteristics of megathrust earthquakes.

Plain Language Summary

Subduction zones host the world's largest earthquakes, which exhibit depth-dependent characteristics such as depletion of high-frequency seismic radiation at shallow depth. Some recent studies propose that elastic properties of wall rocks determine these features despite the fact that fault friction has long been considered to be a dominant factor. Here we design a suite of dynamic earthquake rupture models to explore the roles of wall-rock properties and fault friction. We find that fault friction plays more important roles than wall rock properties in rupture propagation, slip distribution, and high-frequency depletion at shallow depth. On the other hand, even though the low-velocity rock layes decrease rupture velocity to some extent, they enhance and do not reduce high-frequency radiation at shallow depth. We conclude that fault friction plays more important roles than wall-rock properties in depth-dependent rupture characteristics of subduction zone earthquakes.

1 Introduction

Subduction zones host the world's largest earthquakes (Kanamori, 1986). Subduction zone earthquakes exhibit depth-dependent seismic characteristics, such as decrease in normalized source duration with an increase in depth (e.g., Bilek & Lay, 1999), enhanced high frequency radiation as depth increases (e.g., Rushing & Lay, 2012), slower rupture velocity toward the trench for the shallow tsunami earthquakes (Bilek & Lay, 2002), and heterogeneous coseismic slip distribution over different depths (e.g., Ammon et al., 2005; Ide et al., 2011). In particular, recent great earthquakes with wide along-dip rupture extents, such as the 2004 Mw 9.1 Sumatra, 2010 Mw 8.8 Chile, and 2011 Mw 9.0 Tohoku earthquakes, show clearly depth-dependent variations in frequency contents of seismic radiation and slip distribution. High-frequency seismic radiations are imaged in the downdip portions of the megathrusts by large seismic network back-projection methods (e.g., Lay et al., 2010; Kiser and Ishii, 2011; Koper et al., 2012; Ishii, 2011; Lay et al., 2012). Inversions of seismic, geodetic, and tsunami data show that large slip with weak high-frequency seismic radiation occurs in the updip portions of the megathrusts (e.g., Lay et al., 2010; Tong et al., 2010; Ammon et al., 2011; Hayes, 2011; Ide et al., 2011). These features in depth-varying rupture characteristics motivate a four-domain conceptual model for megathrusts (Lay et al., 2012). These four domains are A) near-trench domain where tsunami earthquakes with very weak high-frequency radiation or aseismic slip occur, B) central megathrust domain with large seismic slip and modest high-frequency radiation, C) downdip domain with modest seismic slip and significant coherent high-frequency seismic radiation, and D) transition domain further downdip featuring slow-slip events, low frequency earthquakes and seismic tremor. Although the increase in seismic velocities with depth is recognized to likely cause increasing rupture velocity with depth, the four domains are largely controlled by frictional properties (including seismic, aseismic, and conditionally stable) in the conceptual megathrust model (Lay et al., 2012).

Frictional properties on the plate interface control the wide spectrum of slip behaviors (Scholz, 1998), with diverse observations of ordinary earthquakes, low-frequency earthquakes, and tectonic tremor (Lay, 2015). In a conceptually generic model (Bilek & Lay, 2002; Kodaira et al., 2004; Scholz, 1998) of slip instability at subduction zones, the top several kilometers are in a stable regime, where velocity-strengthening fault conditions dominate. In the seismogenic zone, ranging from the upper limit of ~4 km depth to the lower limit of ~35 km depth, unstable slip and velocity-weakening fault conditions dominate. The downdip stable regime (> 35 km depth) is mainly controlled by velocity-strengthening behaviors. This conceptual model is further supported by experimental evidence, in which frictional properties are depth-varying and temperature dependent (Blanpied et al., 1995; den Hartog & Spiers, 2013), and has been widely used in subduction earthquake simulations (e.g., Im et al., 2020; Liu & Rice, 2005; Liu & Rice, 2007; Meng et al., 2022).

Recently, heterogeneous upper-plate properties are proposed to determine depth-varying rupture behavior of megathrust earthquakes (Sallares and Ranero, 2019; Sallares et al., 2021; Prada et al., 2021). Using 48 P-wave velocity (V_p) models obtained from wide-angel reflection and refraction surveys across circum-Pacific and Indian Ocean subduction zones, Sallares and Ranero (2019) develop a global model of $V_p(z)$. They average V_p at the lower part of the upper plate as a function of interplate boundary depth below seafloor (z) and calculate depth profiles of density ρ(z), S-wave velocity Vs(z), and rigidity μ(z) with experiment-determined empirical relationships of ρ (Vp) and Vs (Vp) (Brocher, 2005). They find that Vp increases by a factor of 2.0-2.5 from ~3.0 km/s at 1 km depth to ~6.5 km/s at 25 km depth, with decreasing gradient downwards. They derive a depth profile of slip based on μ(z), assuming the same rupture area for the same size of earthquakes at different depths. Similarly, they obtain a depth profile of rupture duration based on Vs(z), assuming rupture velocity being 70-90% of Vs. Essentially, slip and rupture duration are inversely proportional to rigidity and Vs, respectively, in their results. Sallares et al. (2021) perform a site-specific study of the 1992 Mw 7.7 Nicaragua tsunami earthquake. They obtain the upper-plate elastic properties from wide-angel reflection and refraction seismic data and multichannel seismic reflection across the rupture area. They also calculate the moment release, slip and stress drop distributions of the earthquake from a finite fault inversion. Consistent with Sallares and Ranero (2019), they emphasize the dominant role of upper-plate elastic properties in controlling large slip and long duration of the event at shallow depth in this tsunami earthquake. Prada et al. (2021) perform 3D dynamic rupture and tsunami simulations to explore the influence of depth-varying upper-plate elastic properties (with a global model developed by Sallares and Raneo, 2019) on rupture characteristics and tsunamigenesis. They compare slip, rupture duration and frequency content from different scenarios with different velocity structures. They use a linear slip-weakening friction law with constant values of friction parameters along the fault, including static and dynamic frictional coefficients and the critical slip distance, for dynamic rupture simulations. Therefore, their dynamic rupture models can be considered as essentially having uniform friction properties along the fault. Their models reproduce depth-varying rupture features in terms of slip, rupture duration and frequency content that agree with Sallares and Ranero (2019).

Both fault frictional properties and wall rock properties are deemed to affect slip instability and dynamic rupture propagation. The heterogeneous coseismic slip of great earthquakes ($M_w \geq 8.0$) along subduction zones appears to be more complicated than that can be explained by a purely frictional or rigidity effect. For instance, the largest coseismic slip can be concentrated near the trench such as in the 2011 M_w 9.0 Tohoku-Oki earthquake (Ide et al., 2011), while some subduction zones exhibit a rupture propagation barrier near the trench such as the 2010 M_w 8.8 Maule earthquake (Lin et al., 2013). This phenomenon implies combined effects of spatial-varying frictional properties and wall rock rigidity. In the classic spring-slider model, slip instability is controlled by the sliding interface's properties (i.e., fault frictional properties) and stiffness of the spring (i.e., surrounding material properties) (Dieterich, 1979; Rice & Ruina, 1983; Scholz, 1998). In dynamic rupture simulations, many studies assume simple velocity structure such as a homogeneous material, partly because they primarily explore effects of heterogeneous friction and/or complex fault geometry on dynamic rupture propagation. Effects of fault-bounding material properties are explored by many other dynamic rupture modeling studies, most notably for bimaterial problems (e.g., Harris and Day, 1997; Andrews and Ben-Zion, 1997; Duan, 2008a; Ampuro and Ben-Zion, 2008) and for low-velocity fault zone problems (e.g., Harris and Day, 1997; Duan, 2008b; Huang and Ampuero, 2011). Nevertheless, effects of heterogeneous velocity structure at subduction zones, in particular shallow low-velocity materials in the upper plate, need to be better understood and incorporated into numerical models of shallow subduction zones. The recent studies by Sallares and Ranero (2019), Sallares et al. (2021), and Prada et al. (2021) make a significant contribution to this endeavor. However, without contrasting and quantifying effects of the two factors, namely fault friction and surrounding material property, in one framework of physics-based models, it is difficult to ascertain which of the two factors plays a more important role, among many other factors such as nonplanar fault geometry and heterogeneous stress state.

There are some studies that incorporate both depth-varying frictional properties and rigidity in dynamic rupture simulations for subduction zone earthquakes. For example, Kozdon and Dunham (2013) perform 2D dynamic rupture simulations of the 2011 Mw 9.0 Tohoku earthquake to understand why and how the rupture could reach the trench. In their models, heterogeneous velocity structure from seismic surveys of the Japan trench (Miura et al., 2001, 2005) is included. They use a rate- and state- dependent friction law (RSF) with velocity-weakening frictional properties for the central portion of the subduction interface. At the shallow portion beneath the accretionary prism, they test several different frictional properties, including velocity-weakening, neutrally stable, and velocity-strengthening. Their preferred model that is validated against seafloor deformation and GPS data shows that the shallow portion of the subduction is velocity strengthening. They find that waves radiated from deep slip reflect off the seafloor, causing large stress changes to the shallow portion of the subduction interface that drive the rupture through the velocity-strengthening region to the trench. Lotto et al. (2017) perform a series of numerical simulations that couple dynamic rupture and tsunami propagation in 2D models to explore compliant prisms' effects on tsunamigenesis. A compliant prism with reduced rigidity is embedded in an otherwise homogeneous material and the shallow portion of the subduction plane beneath the prism has variable frictional properties with velocity-weakening properties at its down-dip extension. They find that increasing prism compliance enhances shallow slip, and that a more velocity-weakening behavior leads to increased slip both beneath the prism and further downdip along the plate boundary fault. Although these studies include both depth-varying friction and rigidity in their dynamic rupture models and shed some lights onto effects of the two factors, they have their specific objectives other than comparing roles of the two factors in rupture dynamics. With the recent series of studies (Sallares and Ranero, 2019; Sallares et al., 2021; Prada et al., 2021) emphasizing a dominant role of depth-varying upper-plate rigidity, it is imperative for the scientific community to better understand roles of the two factors in rupture characteristics of subduction zone earthquakes.

In this study, we compare and quantify the roles of depth-varying frictional properties and rigidity in depth-dependent rupture characteristics of subduction zone earthquakes, using physics-based dynamic rupture models. We include both depth-varying upper-plate rigidity of Sallarès and Ranero (2019) and depth-varying frictional properties along the subduction interface (e.g., Lay, 2015; Lay et al., 2012; Scholz, 1998) in the target model. We also perform dynamic rupture simulations on other comparative models. By contrasting rupture characteristics from these models, we quantify roles of the two factors in determining depth-dependent rupture characteristics observed in recent large subduction zone earthquakes.

2 Methods and Model

2.1 Dynamic rupture simulator

We use the three-dimensional finite element code EQdyna (Duan & Oglesby, 2006; Duan, 2010; Duan, 2012; Luo & Duan, 2018; Liu & Duan, 2018) to simulate a suite of dynamic rupture scenarios. EQdyna is an explicit finite element (FEM) dynamic rupture simulator that has been verified in the Southern California Earthquake Center/U.S. Geological Survey (SCEC/USGS) Spontaneous Rupture Code Verification Project (Harris et al., 2009; Harris et al., 2011; Harris et al., 2018). In this research, seismic waves propagate in an elastic medium and rupture on the fault is governed by the rate-and-state friction law (RSF) with aging law (Dieterich, 1979) implemented in EQdyna (Luo & Duan, 2018) to explore major features of earthquake ruptures in the dynamic phase, following equation (1):

$$\tau = \sigma(f_0 + a\ln\frac{V}{V_0} + b\ln\frac{V_0\theta}{D_c}) \quad (1),$$

where a and b are constitutive frictional parameters determined in laboratory experiments, D_c is the critical slip distance for the exponential healing process after a velocity stepping, and f_0 (set to be 0.6) is a reference friction coefficient associated with a reference steady state slip rate V_0 (set to be 10^{-6} m/s). The state variable, θ, is a description of sliding history and evolves as a function of V, θ, and D_c according to the aging law:

$$\frac{d\theta}{dt} = 1 - \frac{V\theta}{D_c} \quad (2).$$

2.2 Fault geometry and boundary conditions

Our model geometry has length of 190 km along strike, width of 200 km perpendicular to strike, and depth of 50 km. The fault plane dips (ϕ) 15˚ and has both length and width of 150 km (Figure 1). The top boundary of the model (Z = 0) intersects with the free surface, and the side and bottom boundaries are perfectly matched layer (PML) that absorbs seismic waves (Liu & Duan, 2018). The left ($X = X_{min} = -95$ km) and right ($X = X_{max} = 95$ km) boundaries are fixed along X-axis (i.e., zero displacement). We create the finite element (FE) mesh of the model largely using hexahedral elements for computational efficiency, with fault-node-spacing of 200 m. To conform the shallow-dipping ($\phi = 15°$) fault geometry, we cut a hexahedral element into two wedge elements along the fault plane based on the degeneration technique (e.g., Duan, 2010; Duan, 2012; Hughes, 2000; Luo & Duan, 2018). The element sizes around the fault along the x-axis, y-axis, and z-axis are Δx = 200 m, $\Delta y = \Delta x \cos\phi$ = 193 m, and $\Delta z = \Delta x \sin\phi$ = 52 m, respectively.

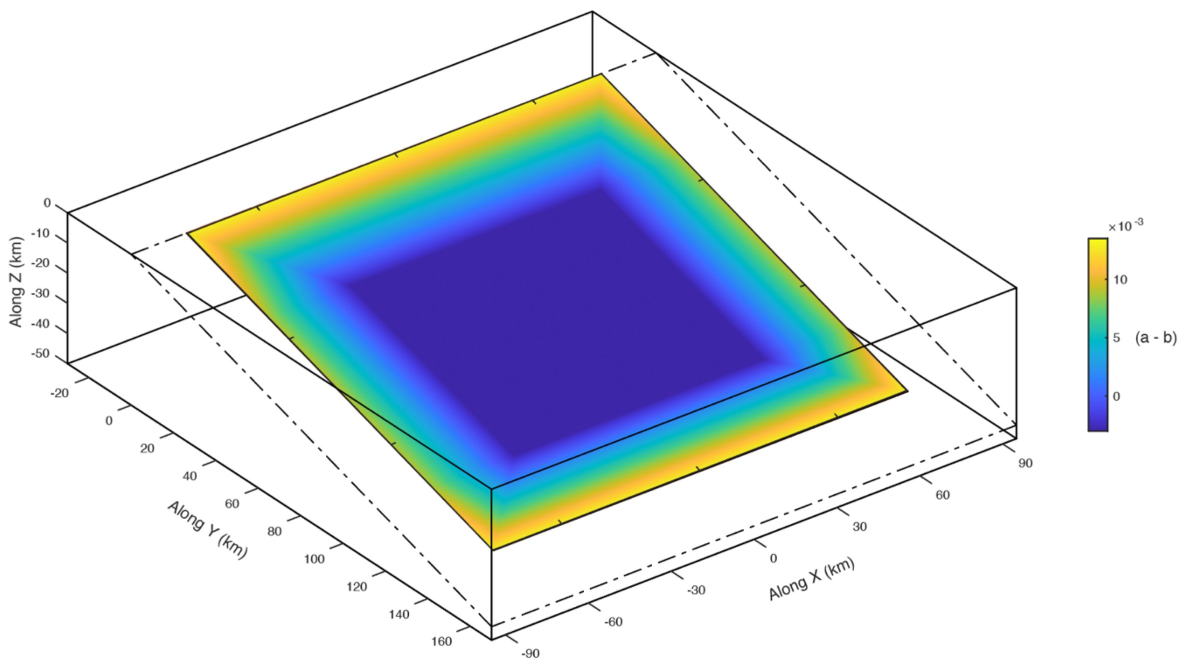

Figure 1. A schematic diagram of three-dimensional fault geometry. On the fault plane, $(a - b)$ for Scenario 3 is shown as an example (L = 40 km; d = 0 km; Figure 2 and Table 1). The dip angle of the fault plane is 15˚. The gap between the colored fault patch and the bounding dashed line is set to be velocity strengthening.

2.3 Parameter choices

Model parameters are explicitly stated in this section. Wherever possible, values of parameters are chosen to match values from appropriate laboratory experiments or field observations. One exception is the critical slip distance D_c: we constrain the parameter mainly based on considerations of computational tractability. We refer to the temperature dependence of the RSF constitutive parameters ($a - b$) for phyllosilicate/quartz-rich fault gouge under hydrothermal conditions reported by den Hartog and Spiers (2013) and a classic characterization of the megathrust frictional environment proposed by Lay (2015).

The transition at the updip from velocity strengthening ($a - b > 0$) to velocity weakening ($a - b < 0$) takes place approximately at 250˚C, corresponding to 10-16 km depth (40-60 km along dip in our models) assuming a geothermal gradient of 16-25˚C/km. We choose a lower bound of ($a - b$) of -0.0030 in the unstable sliding regime (Figure 6a in den Hartog & Spiers, 2013) for our rupture scenarios. We thus construct the depth profile of ($a - b$) as shown in Figure 2a. In addition, we employ an apparent along-strike (or dip) thickness of 30 km (true depth thickness of ~8 km) of a velocity-strengthening layer on left, right, and bottom boundaries of the fault plane to gradually arrest the rupture in our models (white area on the fault plane in Figure 1). The critical slip distance, D_c, is 0.015 m and is homogeneously distributed at all depth. As we will introduce in Section 2.5, we design different scenarios with different apparent thicknesses of updip transition (L) and conditionally stable layer (d) to examine effects of depth-varying friction properties on rupture characteristics (Figures 2a and 3). The ($a - b$) value of a conditionally stable layer is set to be -0.0015 so that it is closer to velocity neutral behavior.

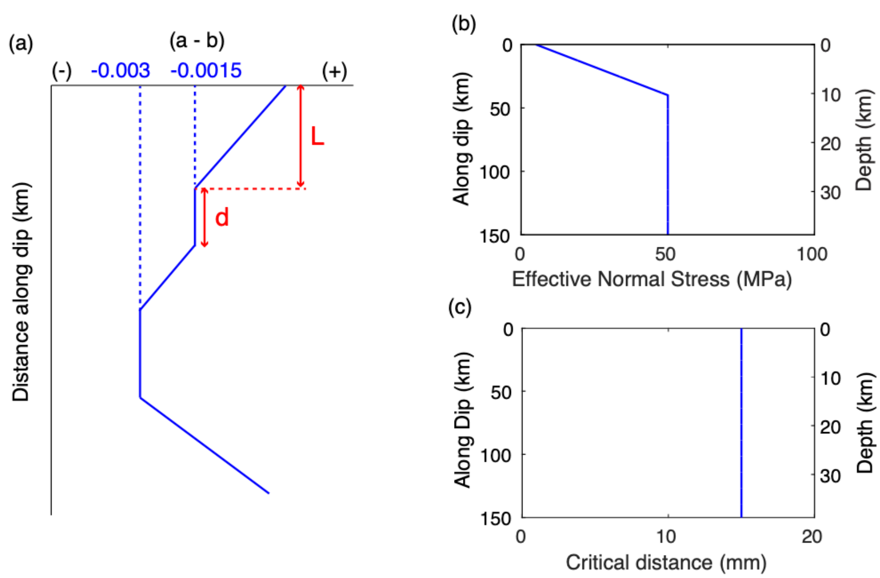

Figure 2. Parameter choices in the rupture scenarios: (a) Depth-varying frictional property of ($a - b$) on fault; L and d denote the apparent along-dip thickness of the updip transition in velocity-dependence behavior and the apparent along-dip thickness of the conditionally stable layer, respectively. The transition from -0.0015 to -0.003 below d has the same ($a - b$) gradient as L. (b) Depth profile of the effective normal stress (σ). (c) Depth profile of the critical distance (D_c).

We assume that the effective normal stress σ to follows an overburden pressure gradient at hydrostatic pore pressure condition from the trench to 40-km along dip (~10 km depth). We also set that σ has a minimum value of 5 MPa at the trench, such that σ gradually increases to 50 MPa at 40-km downdip. Below 40-km downdip, σ is a constant of 50 MPa, assuming an overpressured condition with lithostatic pore-pressure gradient (Rice, 1992) (Figure 2b).

We build two velocity structure models for our dynamic rupture models (Figure 3). One is heterogeneous velocity structure with depth-varying upper-plate P-wave velocity (V_p), S-wave velocity (V_s), and density (ρ) reported by Sallers & Ranero (2019) that are constrained by seismic surveys, and a two-layer velocity structure for the footwall that captures the first-order feature in the downgoing plate. Below 24 km depth in the hanging wall, V_p, V_s, and ρ stay constant at 6.7 km/s, 3.9 km/s, and 2.9 g/cm^3, respectively. The other is homogeneous velocity structure with uniform Vp, Vs, and ρ in the entire model (both the hanging and footwall) with values for those of rocks of the overlying the megathrust at 24-40 km depth.

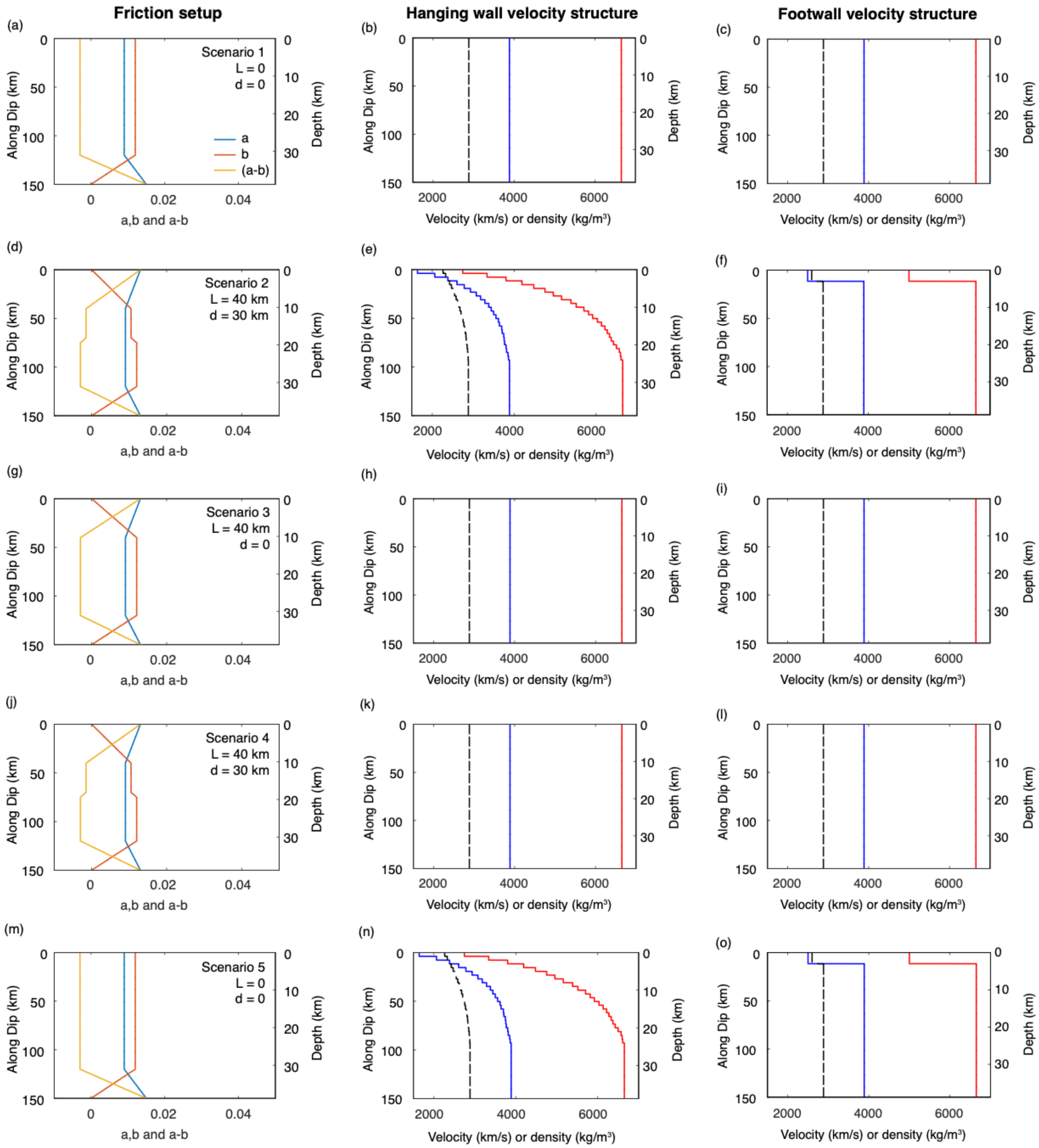

Figure 3. Fault friction and hanging wall velocity structure setup in each scenario. Left panels: friction setup. Middle panels: hanging wall velocity setup. Right panels: footwall velocity setup. Color coding in the middle and right panels: the red curve indicating V_p, blue curve indicating V_s, and black dashed curve indicating density.

2.4 Rupture nucleation and resolution

In the dynamic rupture simulation, a region on the fault with velocity-weakening property is a necessary condition for nucleation. To initiate an instability, this velocity-weakening zone must be larger than a critical nucleation patch size h^*, which is determined by the energy balance of a quasi-statically expanding crack (Lapusta et al., 2000; Rice, 1993; Rubin & Ampuero, 2005). Here, we use an estimation for 3D modeling according to Chen and Lapusta (2009) and Lapusta and Liu (2009):

$$h^* = \frac{\pi}{2}\frac{\mu^* b D_c}{(b-a)^2\sigma} \quad (3),$$

where μ^* is μ for a mode III crack and $\mu/(1-\nu)$ for a mode II crack, μ is the shear modulus, and ν is the Poisson's ratio. In our simulations, we assign a nucleation patch at 110 km along dip with radius of 4 km and slip rate of 0.01 m/s to artificially initiate a rupture event.

During dynamic rupture process, shear stress and slip rate change dramatically in the cohesive zone at the rupture front, which requires a certain number of elements to resolve these features (Day et al., 2005). The spatial resolution of the cohesive zone is thus critical for simulating dynamic rupture propagation (Day et al., 2005), which constrains the element size of the model (e.g., Duan & Day, 2008). The size of the cohesive zone, Λ_0, at rupture speed $v_R = 0^+$ under the RSF law follows

$$\Lambda_0 = C_1\frac{\mu^* L}{b\sigma} \quad (4),$$

where C_1 is a constant of $9\pi/32$ (Lapusta & Liu, 2009). For our FEM scheme, it is found that $\Lambda_0/\Delta x$ of 2.4 with an element size Δx of 200 m can well resolve the cohesive zone (Meng et al., 2022). Taken the parameters choices in *Section 2.3*, we set the model parameters considering equations (3) and (4).

Another consideration for resolution is time step. For dynamic rupture and seismic wave propagation, the time step (dt) is $\alpha d/V_p$, where α is a constant between 0 and 1 and d is the minimum element size (e.g., Liu et al., 2021). Given d = Δz = 52m, V_p = 6.7 km/ s, and α = 0.26, we set dt = 0.002 s.

2.5 Rupture scenarios

Figure 3 shows the fault friction and hanging wall material property setup for five dynamic rupture scenarios. The dynamic rupture scenarios are all nucleated at 110 km. All scenarios incorporate a downdip transition from velocity-weakening behavior at 120-km downdip (depth of ~30 km) to velocity strengthening behavior at 150-km downdip (depth of ~40 km) (white area between the fault patch and the dashed line in Figure 1). To account for the effects of updip transition from velocity-strengthening behavior near the trench to velocity-weakening behavior downdip, we set the along-dip transition distance L, together with a conditionally stable layer with an along-dip distance d (Figure 2a; left panels in Figure 3). For the depth-varying rigidity, we incorporate a multi-layered non-uniform velocity structure of the upper plate following Sallares & Ranero (2019) (middle and right panels in Figure 3). Scenario 1 is a reference scenario that assumes homogeneous velocity structure (Figures 3b and 3c) and homogeneous friction with L of 0 and d of 0 (Figure 3a). Scenario 2, on the other hand, is a most realistic setup that includes depth-varying velocity structure in the hanging wall (Figure 3e) and a two-layer velocity structure footwall (Figure 3f) and depth-varying friction with *L* of 40 km and *d* of 30 km (Figure 3d) among the scenarios. Scenarios 3 and 4 aim to quantify the effects of friction, both with homogeneous velocity structure in the both walls (Figures 3h, 3i, 3k, 3l) and depth varying friction with *L* of 40 km, but different *d* values of 0 km and 30 km (Figures 3g and 3j), respectively. Finally, Scenario 5 aims to quantify the effects of depth-varying rigidity, with depth-varying velocity structure in the hanging wall (Figure 3n) and a two-layer velocity structure footwall (Figure 3o) and homogeneous friction (both *L* and *d* equal 0) (Figure 3m).

3 Results

We present the simulation results of stress drop, total slip, rupture time contours, and rupture velocity on the fault plane in each Scenario. We also analyze the frequency contents of slip rate at selected on-fault stations to examine seismic radiation. We first compare the most realistic model (Scenario 2) and the reference model (Scenario 1) to examine combined effects of the two factors, namely fault friction and upper-plate rigidity. Then we examine other models and compare them with Scenario 1 and/or Scenario 2 to determine roles of the two factors in depth-dependent rupture characteristics.

3.1 Combined effects of depth-varying friction and rigidity on rupture characteristics

We examine the results of Scenarios 1 and 2 for the combined effects of heterogeneous friction and rigidity (Figure 4). The stress change distribution and slip distribution are significantly different between Scenario 1 (homogeneous rigidity and homogeneous friction) and Scenario 2 (heterogeneous rigidity and heterogeneous friction with *L* of 40 km and *d* of 30 km). The stress change distribution on the fault patch in Scenario 1, except for the boundary surrounded by velocity strengthening area (Figure 1), is negative (i.e., stress drop) from downdip toward the trench (Figure 4a). Correspondingly, slip reaches the trench in Scenario 1 with a maximum slip of ~20 m occurring at the trench. On the other hand, in Scenario 2, the updip transition from velocity-weakening behavior downdip to velocity-strengthening behavior updip (*L* of 40 km) diminishes slip at shallow depth, though free surface effects cause some obvious slip at the trench (Figure 4g). The maximum slip of 8m occurs at depth in this scenario. Correspondingly, stress drop (blue) mainly occurs at depth, while stress increases (red) at shallow depth (Figure 4f). Because both heterogeneous fault friction and heterogeneous wall rock properties are included in Scenario 2, we will examine contributions from each of the two factors to the above features in the slip and stress change distributions by other comparative scenarios in the sections below.

Rupture times are direct outputs from our dynamic rupture models. At the rupture time, a fault node reaches a slip rate of 0.01 m/s as the first time during the simulation. Rupture velocities are calculated from rupture times, following a method proposed by (Bizzarri and Das, 2012). In Scenario 1, the rupture time contour (Figure 4c) and the rupture velocity distribution (Figure 4d and 4e) both indicate that the rupture generally accelerates toward the trench from the nucleation patch on a subduction plane with a uniform velocity-weakening friction property embedded in a uniform medium. In Scenario 2, the rupture accelerates within the velocity-weakening patch from the nucleation patch but slows down when it propagates into the conditionally stable part (d of 30 km) and the updip transition patch (L of 40km) (Figure 4h, 4i, and 4j), in particular along the depth profile at along-strike-distance of 50km (black curve in Figure 4j), except near the trench. Supershear rupture occurs near the trench in both scenarios due to effects of free surface and shallow-dipping fault geometry. The slow rupture velocity at shallow depth in Scenario 2 may be attributed to combined effects of updip transition in friction and low-V_p and -V_s at shallow depth. The other comparative scenarios will help clarify and quantify their roles in slower rupture velocity (and thus longer duration) at shallow depth in Scenario 2 than that in Scenario 1.

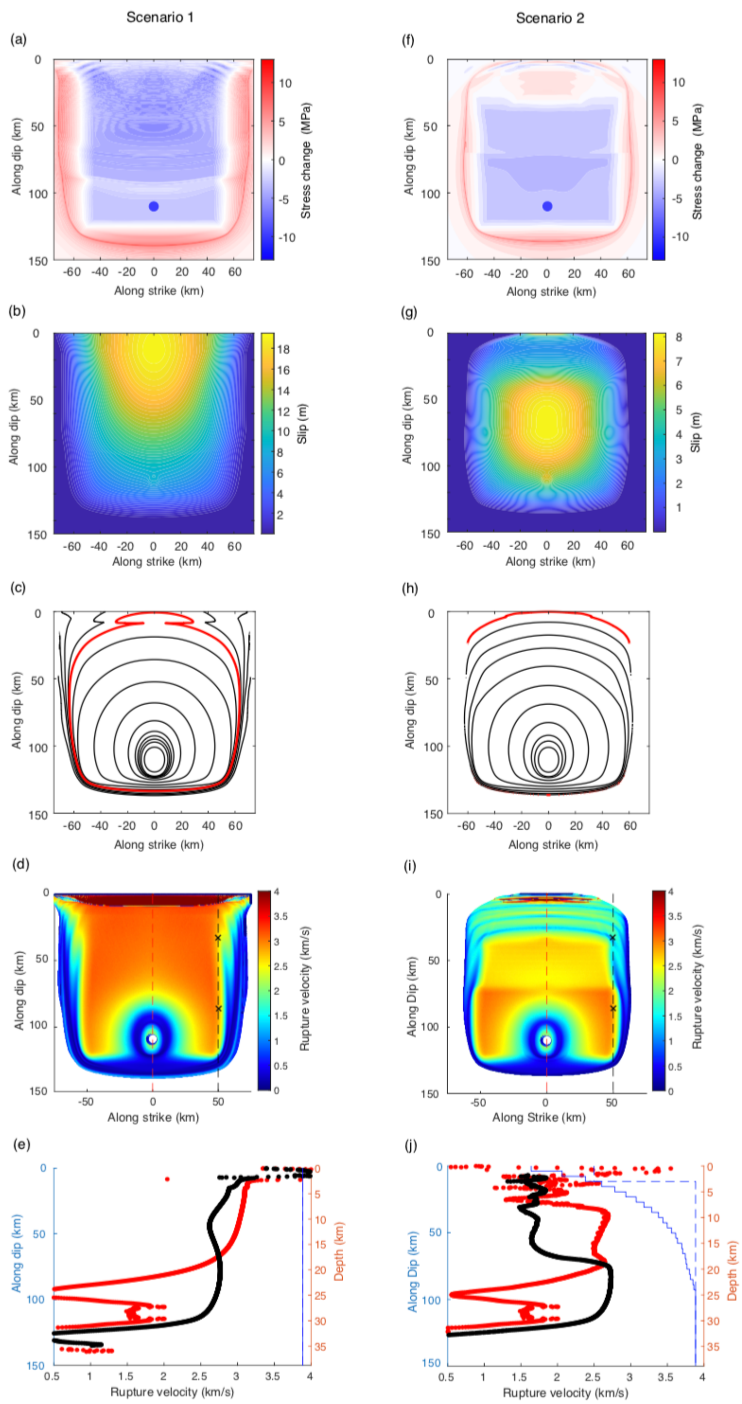

Figure 4. Numerical results of Scenarios 1 (left panels) and 2 (right panels). (a) and (f) show the shear stress change distribution (negative as stress drop); (b) and (g) show the total slip distribution. (c) and (h) show the rupture time contour with an interval of 5 seconds; the red curves indicate that the rupture front reaches the trench at 53 s and 54 s, respectively. (d) and (i) show the rupture velocity distribution. (e) and (j) show the along-dip profiles of rupture velocity along the central line (red line in (d) and (i)) and along 50 km away along-strike from the central line (black line in (d) and (i)). Blue curves in (e) and (j) are shear wave velocity depth profiles in the hanging wall (solid) and footwall (dashed). The crosses in (d) and (i) indicate the locations of the two on-fault stations.

We select two on-fault stations at 8.3 km and 22 km depth (downdip distance of 32 km and 85 km, respectively) along a depth profile at 50 km along-strike distance (Figure 4d or 4i) to examine slip rates and their frequency contents at different depths. Peak slip rate is comparable between the two stations in Scenario 1 (Figure 5a), while it is significant smaller at the shallow station than at the deep station in Scenario 2 (Figure 5c). This contrast is consistent with rupture propagation and slip distribution in the two scenarios analyzed above. Both scenarios show depletion in high frequency content at the shallow station compared with that at the deep station, with Scenario 2 exhibiting a larger amount of depletion (Figure 5b and 5d). Scenario 1 shows high-frequency depletion at the shallow station above ~1 Hz, while that occurs above ~0.2 Hz in Scenario 2, suggesting strong effects in high-frequency depletion at shallow depth form either heterogeneous fault friction, or heterogeneity velocity structure, or both. To direct compare high-frequency depletion at each station from the two scenarios, we plot the amplitude spectra for the shallow station in Figure 5e and the deep station in Figure 5f. By comparing the slopes of the spectra, we can see that Scenario 2 has a larger amount of high-frequency depletion than Scenario 1 at the shallow station for most frequencies above ~0.2 Hz, though there is some complexity at ~2Hz. At the deep station, it appears Scenario 2 radiates more high frequency signals. We will further unravel the roles of heterogeneous friction and rigidity individually on high-frequency depletion in the next two subsections.

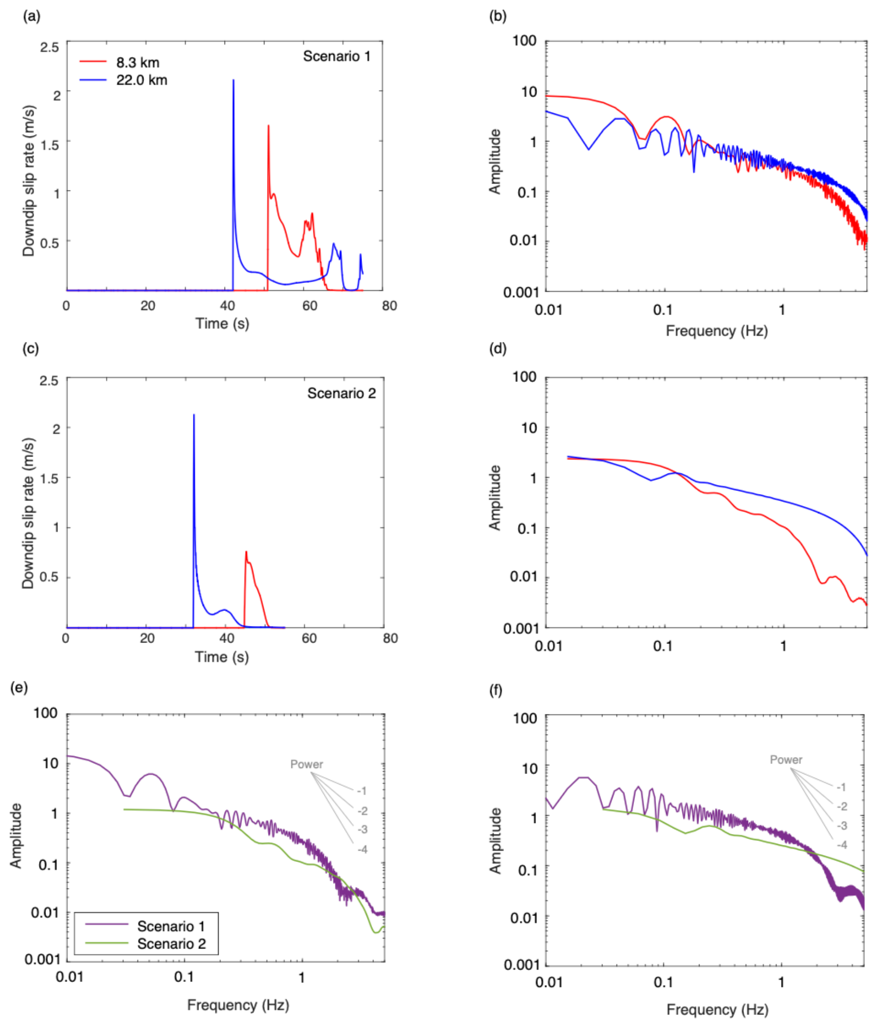

Figure 5. Slip rate and the corresponding frequency content for Scenario 1 (a and b) and Scenario 2 (c and d). Frequency content at 8.3 km (e) and at 22.0 km (f) from the two scenarios are also plotted together for comparison.

3.2 Roles of depth-varying fault friction

Scenario 3 (*L* of 40 km and *d* of 0 km) and Scenario 4 (*L* of 40 km and *d* of 30 km) aim to examine the effects of depth-varying fault friction. Both scenarios exhibit an area of shear stress increase at shallow depth, corresponding to the employment of *L* (Figure 6a and 6b) and diminished slip at shallow depth (Figure 6b and 6g). Scenario 4 shows more subdued slip near the trench and smaller peak slip (~7m) at depth than those in Scenario 3, suggesting additional effects of d of 30km on stress and slip distributions. Overall, slip distribution at shallow depth in both Scenarios 3 and 4 is similar to that in Scenario 2, suggesting the depth-varying fault friction dominates shallow slip distribution if the shallow portion of a subduction plane is velocity strengthening.

In Scenario 3, the rupture time contour (Figure 6c), together with the rupture velocity distribution and the depth profile of rupture velocity (Figure 6d and 6e), show that rupture accelerates toward trench and reaches its maximum near the trench (~4 km/s). Therefore, 40 km along-dip transition thickness (L = 40, Figure 3e) cannot slow down the rupture that initiates at the bottom of the seismogenic zone and accelerates through the zone. In Scenario 4, the rupture does not accelerate much upward from the nucleation patch due to the existence of d=30km (Figure 3g). In addition, the rupture appears more confined along strike direction in Scenario 4 (Figure 6h, 6i, 6j), in particular at shallow depth where the rupture does not break the near-trench area away from the central depth profile. By comparing the rupture velocity along the central depth profile (red curves in Figures 6j and 4e, 4j), we find that the depth-varying friction property in Scenario 4 contributes to rupture slowdown towards the trench to a certain degree, but seems not the dominant factor, in particular for shallow 10 km depth.

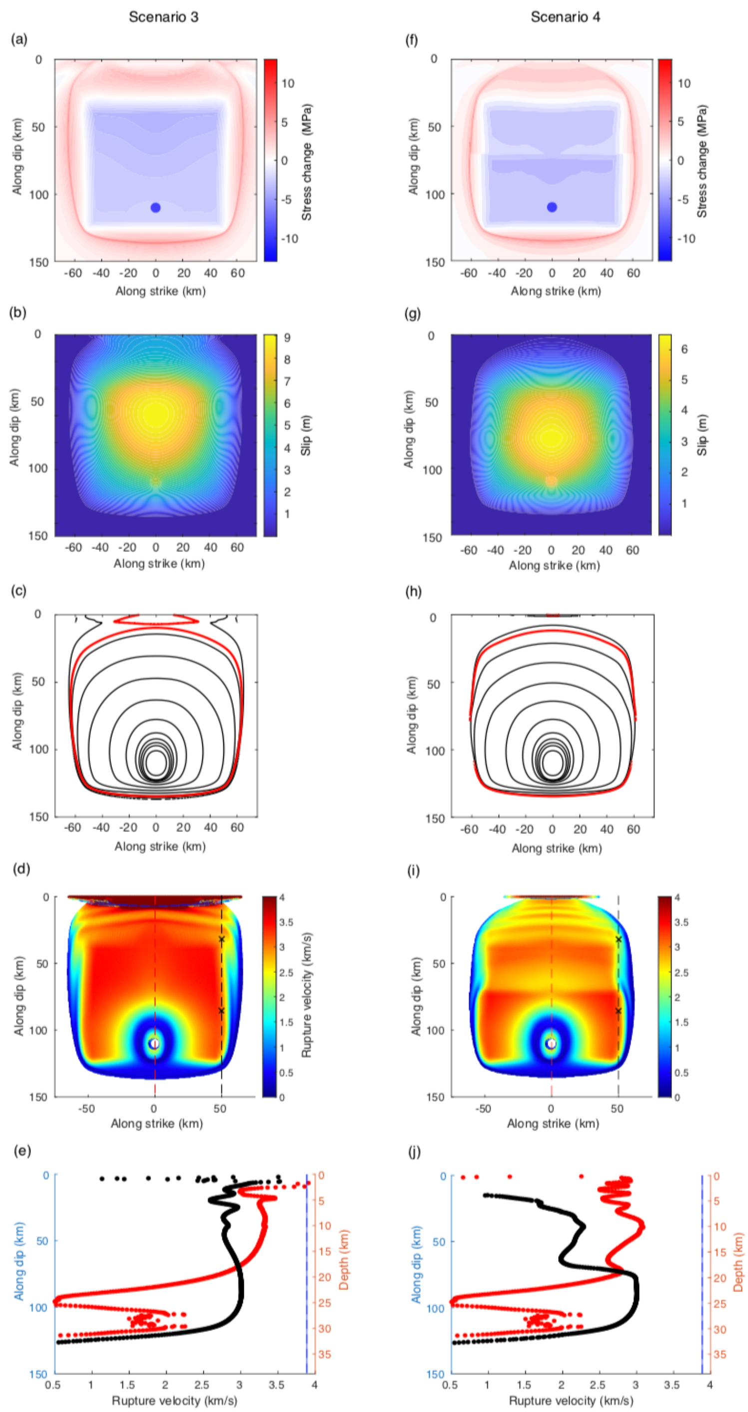

Figure 6. Numerical results of Scenarios 3 (left panels) and 4 (right panels). (a) and (f) show the stress change distribution; (b) and (g) show the total slip distribution. (c) and (h) show the rupture time contour with an interval of 5 seconds; the red curves indicate that the rupture front reaches the trench at 51.5 s and 53.5 s, respectively. (d) and (i) show the rupture velocity distribution. (e) and (j) show the along-dip profiles of rupture velocity along the central line (red line in (d) and (i)) and along 50 km away along-strike from the central line (black line in (d) and (i)). The crosses in (d) and (i) indicate the locations of the two on-fault stations.

Two stations at depth of 8.3 km and 22 km in both Scenarios show that peak slip rate significantly decreases toward the trench (Figure 7a and 7c) and that high-frequency content depletes at the shallow station (Figure 7b and 7d). With an employment of d = 30km, frequency content between 0.5 and 3 Hz depletes more in Scenario 4 than in Scenario 3 (Figure 7e). It appears that the depth-varying fault friction properties in Scenarios 3 and 4 dominate high-frequency depletion at shallow depth.

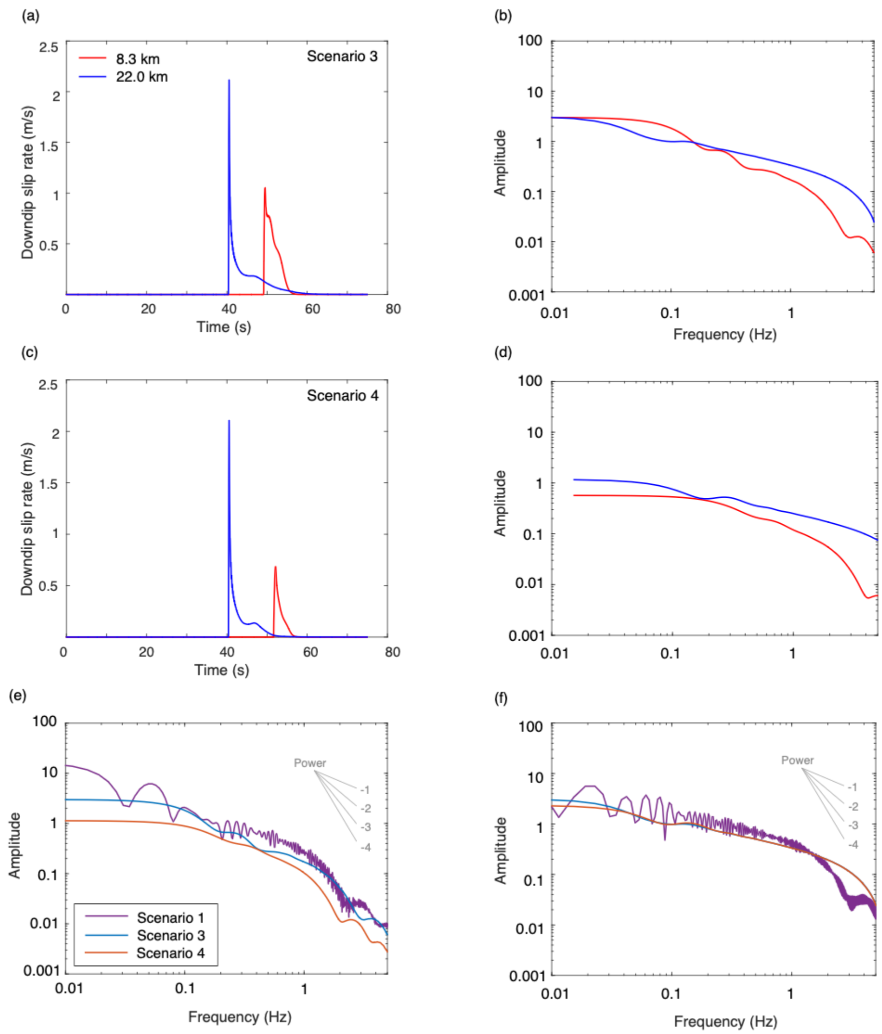

Figure 7. Slip rate and the corresponding frequency content for Scenario 3 (a and b) and Scenario 4 (c and d). Frequency contents at 8.3 km (e) and at 22.0 km (f) are compared among these two scenarios and Scenario 1.

3.3 Roles of depth-varying upper-plate rigidity

We examine the role of depth-varying upper-plate rigidity in Scenario 5 (heterogeneous velocity structure and homogeneous friction with *L* of 0 and *d* of 0). Similar to Scenario 1, Scenario 5 exhibits a large stress drop up to the trench (Figure 8a) and the large slip is concentrated near the trench (Figure 8b). In particular, this scenario produces a maximum slip > 50 m at the trench (Figure 8b), which is much larger than all other scenarios, including Scenario 1. This result is intuitive because as the wall rock becomes less rigid, the trenchward portion becomes more compliant. Thus, more slip is generated under the same amount of stress drop. Comparing with the other scenarios, this scenario suggests that low-velocity rock layers in the upper plate dominates total amount of shallow slip, if the shallow portion of a subduction plane is velocity-weakening.

The rupture propagation features show that, except for the initial increase in rupture velocity at the deep part of the subduction plane and the trench portion, rupture velocity generally ranges from 2-3 km/s (Figure 8d and 8e). The near-trench rupture velocity significantly exceeds V_s in both hanging wall and footwall (i.e., supershear rupture), indicating that an employment of low- velocity upper plate layers do not fully cap the rupture velocity, due to the effects of free surface and shallow-dipping fault geometry. Comparing with other scenarios (e.g., rupture velocity along the central profile in all scenarios), we can find that the upper-plate low-velocity layers contribute significantly to slow rupture at a narrow range of shallow depth (e.g., 1-3 km depth).

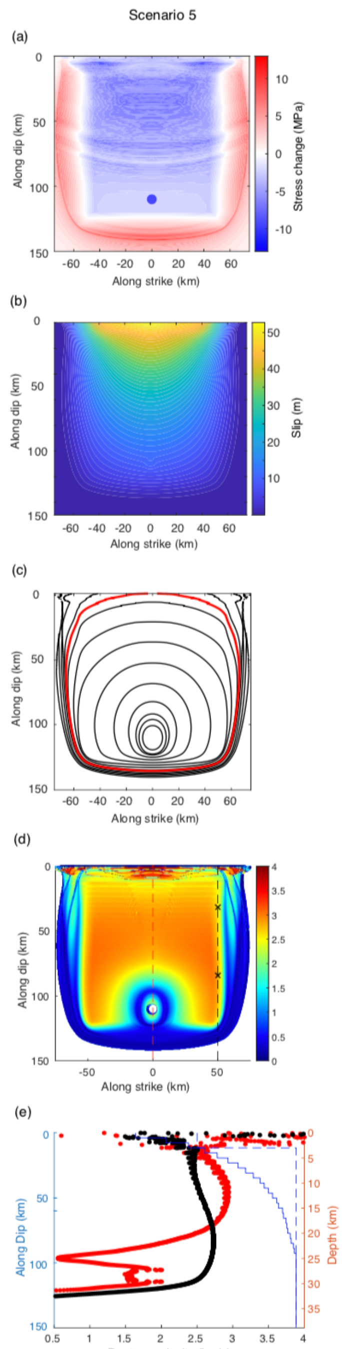

Figure 8. Numerical results of Scenario 5. (a) shows the stress change distribution; (b) shows the total slip distribution. (c) shows the rupture time contour with an interval of 5 seconds; the red curves indicate that the rupture front reaches the trench at 47.5 s. (d) shows the rupture velocity distribution. (e) shows the along-dip profiles of rupture velocity along the central line (red line in (d)) and along 50 km away along-strike from the central line (black line in (d)). The crosses in (d) and indicate the locations of the two on-fault stations.

Slip rate time histories (Figure 9a) at the two stations from this scenario show that the shallow station has similar peak slip rate with more high-frequency signals compared with the deep station (Figure 9b). The amplitude spectra at the two stations from this scenario does not show clear high-frequency depletion at the shallow station compared with the deep station, also in contrast to all other scenarios. Comparing with Scenario 1 at the shallow station (Figure 9c), the upper plate low-velocity layers enhance high-frequency seismic radiation at shallow depth, in contrast to causing high-frequency depletion there in other scenarios. Comparing with Scenario 2 at the shallow station (Figure 9e), in conjunction with Figure 5e, we find that it is the high-frequency enhancement from the low-velocity layers that cause a complex feature at ~2Hz in high-frequency depletion in Scenario 2, as described in an earlier section. Scenario 2 has both depth-varying fault friction and depth-varying velocity structure. The former causes significant high-frequency depletion at the shallow station, while the latter cause high-frequency enhancement. At most frequencies above ~0.2 Hz, high-frequency depletion from depth-varying fault friction dominates over high-frequency enhancement from depth-varying velocity structure, except at ~ 2 Hz. At the deep station, Scenario 5 is also rich in high frequency content comparing to Scenario 1 (Figure 9d), while it is more depleted in high frequency content comparing to Scenario 2 at frequency > 2 Hz (Figure 9f).

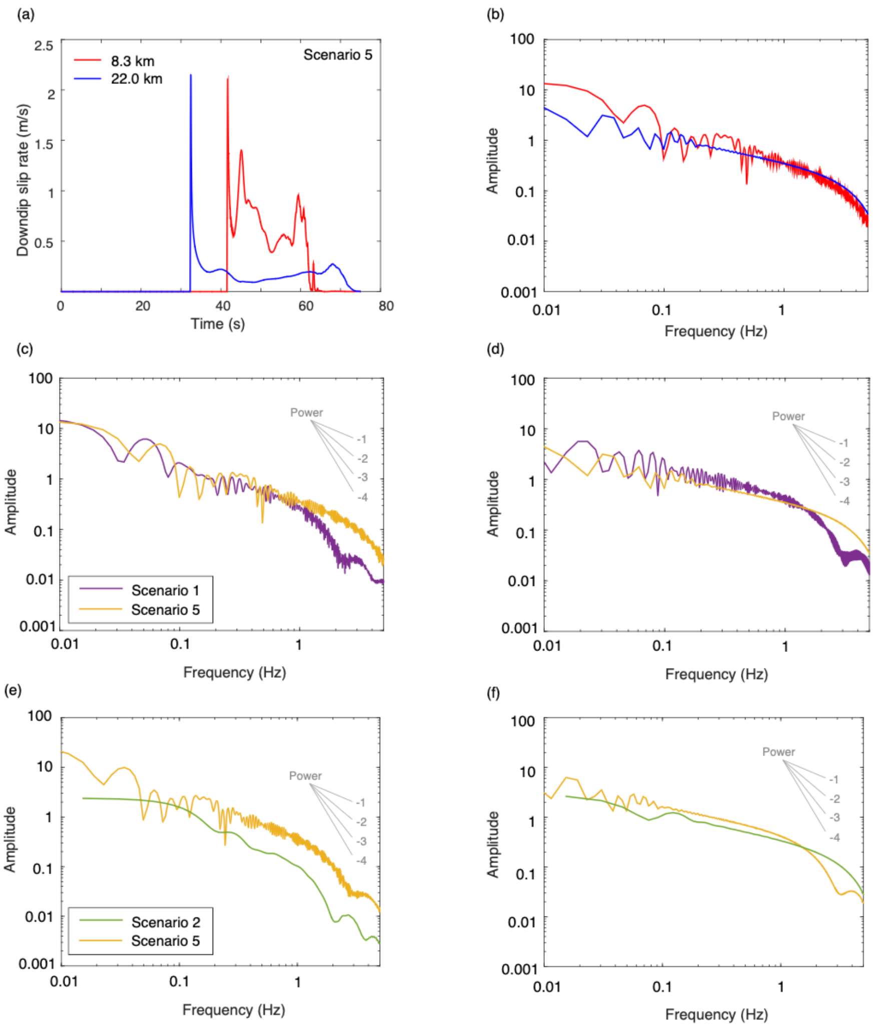

Figure 9. Slip rate and the corresponding frequency content for Scenario 5 (a and b) at 8.3 km and 22.0 km depth stations. Comparison between Scenarios 1 and 5 with frequency content at 8.3 km (c) and at 22.0 km (d), as well as comparison between Scenarios 2 and 5 with frequency content at 8.3 km (e) and at 22.0 km (f) are shown.

4 Discussion

Our numerical simulations on rupture scenarios reveal that the updip transition layer *L* from velocity-strengthening behavior near the trench to velocity-weakening behavior downdip suppresses rupture propagation toward the trench. With an employment of a conditionally stable layer *d*, total slip and rupture velocity significantly decreases, resulting in a longer rupture duration as *d* increases. As the low-velocity layer leads to a more compliant material near the trench, total slip is significantly higher in the scenarios with heterogeneous velocity structure (Scenarios 2 and 5). Imposing depth-varying friction promotes trenchward decrease in slip rate, as well as depletion in high-frequency radiation at shallow depth (Scenarios 3 and 4).

We identify that the slip distribution may highly depend on depth-varying rigidity, where a more compliant material leads to a larger total slip. In Figure 10, we further quantify the total slip distribution by normalizing all the Scenarios 2 through 5 over Scenario 1 (Figure 10). With *L*, *d*, as well as a uniform velocity structure employed, total slip ratio is less than 0.7 and more concentrated near the nucleation patch (Figure 10a-10c). In contrast, Scenario 5 has the largest slip ratio of 3 near the trench (Figure 10d). We summarize that while the amount of total slip is controlled by depth-varying rigidity, whereas the pattern of concentration is controlled by friction.

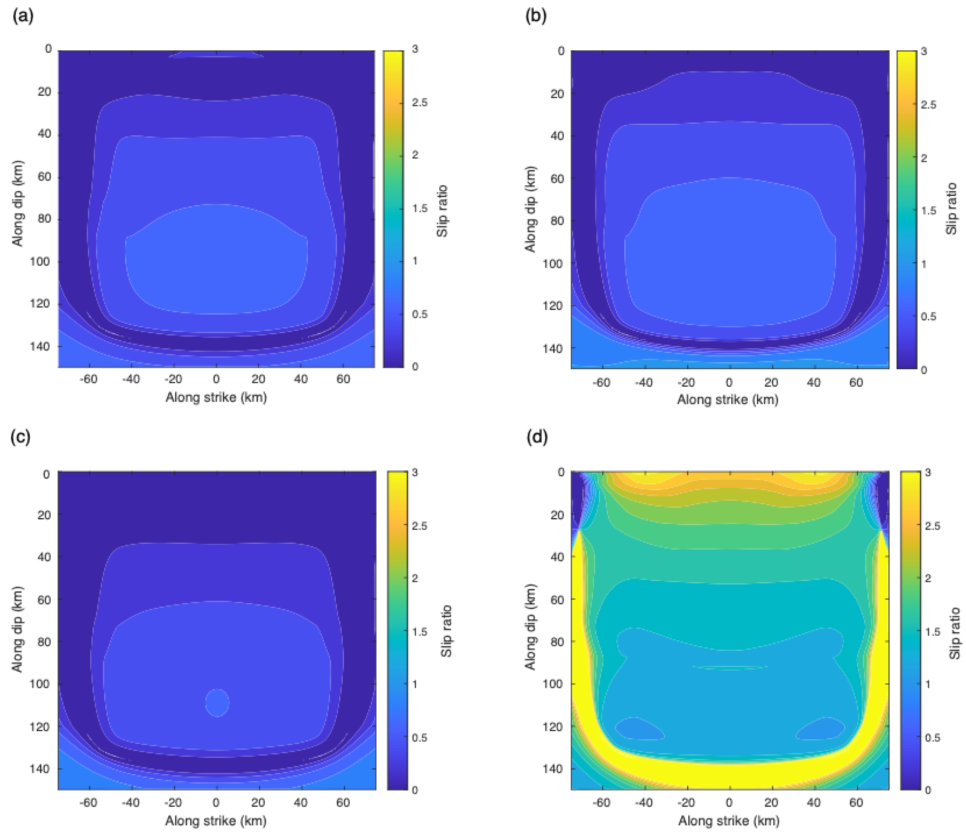

Figure 10. Total slip distribution normalized to Scenario 1: (a) Scenario 2, (b) Scenario 3, (c) Scenario 4, (d) Scenario 5. The contour interval is 0.2.

In subduction zone earthquakes where largest coseismic slip concentrated near the trench, such as in the 2011 Mw 9.0 Tohoku-Oki earthquake (Ide et al., 2011), the friction and the rigidity may be close to our Scenario 5 (homogeneous friction and heterogeneous velocity structure), though some thin layer of velocity strengthening may exist, as proposed by Kozdon and Dunham (2013) and Lotto et al. (2017). While some subduction zones exhibit a rupture propagation barrier near the trench such as the 2010 M_w 8.8 Maule earthquake (Lin et al., 2013), we expect that depth-varying friction plays a dominant role, which is similar to our Scenarios 3 and 4 (heterogeneous friction and homogeneous velocity structure), or considering a realistic upper-plate rigidity (e.g., Sallares & Ranero, 2019), closer to our Scenario 2 (heterogeneous friction and heterogeneous velocity structure).

We address the effects of heterogeneous velocity structure, in particular the low-velocity layer in the shallow portion in Scenarios 2 and 5. An updip low-velocity zone is equivalent to a compliant accretionary prism, which yields a larger slip near the trench. This observation is consistent with the results reported by Lotto et al. (2017). Although we do not focus on varying $a - b$ in the unstable regime, we agree with Lotto et al. (2017) that a more velocity-weakening friction enhances final overall slip, in that a more velocity-weakening prism induces a larger stress drop (equation (1)) and results in a larger total slip. In addition, the wall rock in our numerical simulations is elastic. We remark that plastic yielding in a compliant accretionary prism can slow down rupture propagation and enhance seafloor displacement, as reported by Ma (2012) and Ma and Hirakawa (2013).

This study examines and compares roles of depth-varying fault friction and heterogeneous upper-plate material properties in depth-dependent rupture characteristics of megathrust earthquakes that rupture the entire seismogenic zone. In a separate study, Meng and Duan (2022) explore roles of heterogeneous fault friction and heterogenous upper-plate material properties in rupture characteristics of tsunami earthquakes that occur on shallow portions of subduction planes and generate abnormally large tsunami waves. In their heterogeneous fault friction models, they introduce asperities (unstable patches) with strongly velocity-weakening friction properties embedded in a weakly velocity-weakening conditionally stable zone. Their findings corroborate our results obtained in this study, including (1) the dominant roles of fault friction in slow rupture speed (and thus long rupture duration) and high-frequency depletion at shallow depth and (2) heterogeneous upper-plate material properties mainly contributing to large slip near the trench.

5 Conclusions

We design five rupture scenarios to quantify the effects of depth-varying fault friction and heterogeneous upper-plate rigidity on dynamics of megathrust earthquakes. Our numerical simulations on rupture scenarios reveal that the updip transition from velocity-strengthening behavior near the trench to velocity-weakening behavior downdip suppresses rupture propagation toward the trench and a thicker velocity-strengthening layer results in a more confined total slip at depth. With employment of a conditionally stable layer, total slip and rupture velocity significantly decreases, resulting in a longer rupture duration as the thickness of the conditionally stable layer increases. As the low-velocity zone leads to a more compliant medium near the trench, total slip is significantly higher in the scenarios with low-velocity upper-plate layers. Slip rate history and its frequency content show that depth-varying fault friction dominates high-frequency depletion at shallow depth, whereas depth-varying rigidity enhances high-frequency radiation. We conclude that fault friction plays more important roles than wall-rock properties in depth-dependent rupture characteristics of megathrust earthquakes.

Acknowledgments

The authors thank Texas A&M University High Performance Research Computing (https://hprc.tamu.edu) for the advanced computer resources used in this study.

Data Availability

The datasets used in generating the model setups for each scenario (Figure 3) and time series of slip rate at the two on-fault stations (Figures 5, 7, and 9) are available at the Zenodo Repository (https://doi.org/10.5281/zenodo.6643024). Please contact the corresponding author for software availability.

References

Ammon, C. J., Ji, C., Thio, H.-K., Robinson, D., Ni, S., Hjorleifsdottir, V., et al. (2005). Rupture process of the 2004 Sumatra-Andaman earthquake. *Science*, *308*(5725), 1133–1139. https://doi.org/10.1126/science.1112260

Ampuero, J.-P., & Ben-Zion, Y. (2008). Cracks, pulses and macroscopic asymmetry of dynamic rupture on a bimaterial interface with velocity-weakening friction. *Geophysical Journal International*, *173*(2), 674–692. https://doi.org/10.1111/j.1365-246X.2008.03736.x

Andrews, D. J., & Ben-Zion, Y. (1997). Wrinkle-like slip pulse on a fault between different materials. *Journal of Geophysical Research: Solid Earth*, *102*(B1), 553–571. https://doi.org/10.1029/96JB02856

Bilek, S. L., & Lay, T. (2002). Tsunami earthquakes possibly widespread manifestations of frictional conditional stability: Variability of greenland accumulation. *Geophysical Research Letters*, *29*(14), 18-1–18-4. https://doi.org/10.1029/2002GL015215

Bilek, S. L., & Lay, T. (1999). Rigidity variations with depth along interplate megathrust faults in subduction zones. *Nature*, *400*(6743), 443–446. https://doi.org/10.1038/22739

Bizzarri, A., & Das, S. (2012). Mechanics of 3-D shear cracks between Rayleigh and shear wave rupture speeds. *Earth and Planetary Science Letters*, *357-358*, 397-404. https://doi.org/10.1016/j.epsl.2012.09.053

Blanpied, M. L., Lockner, D. A., & Byerlee, J. D. (1995). Frictional slip of granite at hydrothermal conditions. *Journal of Geophysical Research: Solid Earth*, *100*(B7), 13045–13064. https://doi.org/10.1029/95JB00862

Brocher, T. M. (2005). Empirical relations between elastic wavespeeds and density in the Earth's crust. *Bulletin of the Seismological Society of America*, *95*(6), 2081–2092. https://doi.org/10.1785/0120050077

Chen, T., & Lapusta, N. (2009). Scaling of small repeating earthquakes explained by interaction of seismic and aseismic slip in a rate and state fault model: Simulations of repeating earthquakes. *Journal of Geophysical Research: Solid Earth*, *114*(B1). https://doi.org/10.1029/2008JB005749

Day, S. M., Dalguer, L. A., Lapusta, N., & Liu, Y. (2005). Comparison of finite difference and boundary integral solutions to three-dimensional spontaneous rupture. *Journal of Geophysical Research*, *110*(B12), B12307. https://doi.org/10.1029/2005JB003813

Dieterich, J. H. (1979). Modeling of rock friction: 1. Experimental results and constitutive equations. *Journal of Geophysical Research*, *84*(B5), 2161–2168. https://doi.org/10.1029/JB084iB05p02161

Duan, B. (2010). Role of initial stress rotations in rupture dynamics and ground motion: A case study with implications for the Wenchuan earthquake. *Journal of Geophysical Research*, *115*(B5), B05301. https://doi.org/10.1029/2009JB006750

Duan, B. (2012). Dynamic rupture of the 2011 Mw 9.0 Tohoku-Oki earthquake: Roles of a possible subducting seamount. *Journal of Geophysical Research: Solid Earth*, *117*(B5), n/a-n/a. https://doi.org/10.1029/2011JB009124

Duan, B., & Day, S. M. (2008). Inelastic strain distribution and seismic radiation from rupture of a fault kink. *Journal of Geophysical Research*, *113*(B12), B12311. https://doi.org/10.1029/2008JB005847

Duan, B., & Oglesby, D. D. (2006). Heterogeneous fault stresses from previous earthquakes and the effect on dynamics of parallel strike-slip faults: Heterogeneous stress on parallel faults. *Journal of Geophysical Research: Solid Earth*, *111*(B5), B05309. https://doi.org/10.1029/2005JB004138

Harris, R. A., Barall, M., Archuleta, R., Dunham, E., Aagaard, B., Ampuero, J. P., et al. (2009). The SCEC/USGS dynamic earthquake rupture code verification exercise. *Seismological Research Letters*, *80*(1), 119–126. https://doi.org/10.1785/gssrl.80.1.119

Harris, R. A., Barall, M., Andrews, D. J., Duan, B., Ma, S., Dunham, E. M., et al. (2011). Verifying a computational method for predicting extreme ground motion. *Seismological Research Letters*, *82*(5), 638–644. https://doi.org/10.1785/gssrl.82.5.638

Harris, Ruth A., Barall, M., Aagaard, B., Ma, S., Roten, D., Olsen, K., et al. (2018). A suite of exercises for verifying dynamic earthquake rupture codes. *Seismological Research Letters*, *89*(3), 1146–1162. https://doi.org/10.1785/0220170222

Harris, R. A., & Day, S. M. (1997). Effects of a low-velocity zone on a dynamic rupture. *Bulletin of the Seismological Society of America*, *87*(5), 1267–1280. https://doi.org/10.1785/BSSA0870051267 den Hartog, S. A. M., & Spiers, C. J. (2013). Influence of subduction zone conditions and gouge composition on frictional slip stability of megathrust faults. *Tectonophysics*, *600*, 75–90. https://doi.org/10.1016/j.tecto.2012.11.006

Hayes, G. P. (2011). Rapid source characterization of the 2011 M w 9.0 off the Pacific coast of Tohoku Earthquake. *Earth, Planets and Space*, *63*(7), 529–534. https://doi.org/10.5047/eps.2011.05.012

Huang, Y., & Ampuero, J.-P. (2011). Pulse-like ruptures induced by low-velocity fault zones. *Journal of Geophysical Research*, *116*, B12307. https://doi.org/10.1029/2011JB008684

Hughes, T. J. R. (2000). *The finite element method: linear static and dynamic finite element analysis*. Mineola, NY: Dover Publications.

Ide, S., Baltay, A., & Beroza, G. C. (2011). Shallow dynamic overshoot and energetic deep rupture in the 2011 mw 9.0 Tohoku-Oki earthquake. *Science*, *332*(6036), 1426–1429. https://doi.org/10.1126/science.1207020

Im, K., Saffer, D., Marone, C., & Avouac, J.-P. (2020). Slip-rate-dependent friction as a universal mechanism for slow slip events. *Nature Geoscience*, *13*(10), 705–710. https://doi.org/10.1038/s41561-020-0627-9

Ishii, M. (2011). High-frequency rupture properties of the M w 9.0 off the Pacific coast of Tohoku Earthquake. *Earth, Planets and Space*, *63*(7), 609–614. https://doi.org/10.5047/eps.2011.07.009

Kanamori, H. (1986). Rupture process of subduction-zone earthquakes. *Annual Review of Earth and Planetary Sciences*, *14*(1), 293–322. https://doi.org/10.1146/annurev.ea.14.050186.001453

Kaneko, Y., Lapusta, N., & Ampuero, J.-P. (2008). Spectral element modeling of spontaneous earthquake rupture on rate and state faults: Effect of velocity-strengthening friction at shallow depths. *Journal of Geophysical Research*, *113*(B9), B09317. https://doi.org/10.1029/2007JB005553

Kiser, E., & Ishii, M. (2011). The 2010 Mw 8.8 Chile earthquake: Triggering on multiple segments and frequency-dependent rupture behavior: The 2010 Mw 8.8 Chile earthquake. *Geophysical Research Letters*, *38*(7), L07301. https://doi.org/10.1029/2011GL047140

Kodaira, S., Iidaka, T., Kato, A., Park, J.-O., Iwasaki, T., & Kaneda, Y. (2004). High pore fluid pressure may cause silent slip in the Nankai Trough. *Science*, *304*(5675), 1295–1298. https://doi.org/10.1126/science.1096535

Koper, K. D., Hutko, A. R., Lay, T., & Sufri, O. (2012). Imaging short-period seismic radiation from the 27 February 2010 Chile (M_W 8.8) earthquake by back-projection of *P* , *PP* , and *PKIKP* waves: Rupture imaging of 2010 Chile earthquake. *Journal of Geophysical Research: Solid Earth*, *117*, B02308. https://doi.org/10.1029/2011JB008576

Kozdon, J. E., & Dunham, E. M. (2013). Rupture to the trench: Dynamic rupture simulations of the 11 March 2011 Tohoku Earthquake. *Bulletin of the Seismological Society of America*, *103*(2B), 1275–1289. https://doi.org/10.1785/0120120136

Lapusta, N., & Liu, Y. (2009). Three-dimensional boundary integral modeling of spontaneous earthquake sequences and aseismic slip. *Journal of Geophysical Research*, *114*(B9), B09303. https://doi.org/10.1029/2008JB005934

Lapusta, N., Rice, J. R., Ben-Zion, Y., & Zheng, G. (2000). Elastodynamic analysis for slow tectonic loading with spontaneous rupture episodes on faults with rate- and state-dependent friction. *Journal of Geophysical Research: Solid Earth*, *105*(B10), 23765–23789. https://doi.org/10.1029/2000JB900250

Lay, T. (2015). The surge of great earthquakes from 2004 to 2014. *Earth and Planetary Science Letters*, *409*, 133–146. https://doi.org/10.1016/j.epsl.2014.10.047

Lay, T., Ammon, C. J., Kanamori, H., Koper, K. D., Sufri, O., & Hutko, A. R. (2010). Teleseismic inversion for rupture process of the 27 February 2010 Chile (M_w 8.8) earthquake: The 2010 great Chile earthquake rupture. *Geophysical Research Letters*, *37*(13), L13301. https://doi.org/10.1029/2010GL043379

Lay, T., Kanamori, H., Ammon, C. J., Koper, K. D., Hutko, A. R., Ye, L., et al. (2012). Depth-varying rupture properties of subduction zone megathrust faults: Megathrust rupture domains. *Journal of Geophysical Research: Solid Earth*, *117*, B04311. https://doi.org/10.1029/2011JB009133

Lin, Y. N., Sladen, A., Ortega-Culaciati, F., Simons, M., Avouac, J.-P., Fielding, E. J., et al. (2013). Coseismic and postseismic slip associated with the 2010 Maule earthquake, Chile: Characterizing the Arauco Peninsula barrier effect. *Journal of Geophysical Research: Solid Earth*, *118*(6), 3142–3159. https://doi.org/10.1002/jgrb.50207

Liu, D., & Duan, B. (2018). Scenario earthquake and ground-motion simulations in North China: Effects of heterogeneous fault stress and 3D basin structure. *Bulletin of the Seismological Society of America*, *108*(4), 2148–2169. https://doi.org/10.1785/0120170374

Liu, D., Duan, B., Prush, V. B., Oskin, M. E., & Liu-Zeng, J. (2021). Observation-constrained multicycle dynamic models of the Pingding Shan earthquake gate along the Altyn Tagh Fault. *Tectonophysics*, *814*, 228948. https://doi.org/10.1016/j.tecto.2021.228948

Liu, Y., & Rice, J. R. (2005). Aseismic slip transients emerge spontaneously in three-dimensional rate and state modeling of subduction earthquake sequences. *Journal of Geophysical Research*, *110*(B8), B08307. https://doi.org/10.1029/2004JB003424

Liu, Y., & Rice, J. R. (2007). Spontaneous and triggered aseismic deformation transients in a subduction fault model. *Journal of Geophysical Research*, *112*(B9), B09404. https://doi.org/10.1029/2007JB004930

Lotto, G. C., Dunham, E. M., Jeppson, T. N., & Tobin, H. J. (2017). The effect of compliant prisms on subduction zone earthquakes and tsunamis. *Earth and Planetary Science Letters*, *458*, 213–222. https://doi.org/10.1016/j.epsl.2016.10.050

Luo, B., & Duan, B. (2018). Dynamics of nonplanar thrust faults governed by various friction laws. *Journal of Geophysical Research: Solid Earth*, *123*(6), 5147–5168. https://doi.org/10.1029/2017JB015320

Luo, B., Duan, B., & Liu, D. (2020). 3D finite-element modeling of dynamic rupture and aseismic slip over earthquake cycles on geometrically complex faults. *Bulletin of the Seismological Society of America*, *110*(6), 2619–2637. https://doi.org/10.1785/0120200047

Ma, S. (2012). A self-consistent mechanism for slow dynamic deformation and tsunami generation for earthquakes in the shallow subduction zone: Slow rupture and tsunami generation. *Geophysical Research Letters*, *39*(11), L11310. https://doi.org/10.1029/2012GL051854

Ma, S., & Hirakawa, E. T. (2013). Dynamic wedge failure reveals anomalous energy radiation of shallow subduction earthquakes. *Earth and Planetary Science Letters*, *375*, 113–122. https://doi.org/10.1016/j.epsl.2013.05.016

Meng, Q., & Duan, B. (2022). Do upper-plate material properties or fault frictional properties dominate tsunami earthquake characteristics? https://doi.org/10.1002/essoar.10511617.1

Meng, Q., Duan, B., & Luo, B. (2022). Using a dynamic earthquake simulator to explore tsunami earthquake generation. *Geophysical Journal International*, *229*(1), 255–273. https://doi.org/10.1093/gji/ggab470

Miura, S., Takahashi, N., Nakanishi, A., Ito, S., Kodaira, S., Tsuru, T., & Kaneda, Y. (2001). Seismic velocity structure off Miyagi fore-arc region, Japan Trench, using ocean bottom seismographic data. *Frontier Research of Earth Evolution*, *1*, 337–340.

Miura, S., Takahashi, N., Nakanishi, A., Tsuru, T., Kodaira, S., & Kaneda, Y. (2005). Structural characteristics off Miyagi forearc region, the Japan Trench seismogenic zone, deduced from a wide-angle reflection and refraction study. *Tectonophysics*, *407*(3–4), 165–188. https://doi.org/10.1016/j.tecto.2005.08.001

Prada, M., Galvez, P., Ampuero, J., Sallarès, V., Sánchez-Linares, C., Macías, J., & Peter, D. (2021). The influence of depth-varying elastic properties of the upper plate on megathrust earthquake rupture dynamics and tsunamigenesis. *Journal of Geophysical Research: Solid Earth*, *126*(11). https://doi.org/10.1029/2021JB022328

Rice, J. R., & Ruina, A. L. (1983). Stability of steady frictional slipping. *Journal of Applied Mechanics*, *50*(2), 343–349. https://doi.org/10.1115/1.3167042

Rice, J. R. (1992). Chapter 20 Fault stress states, pore pressure distributions, and the weakness of the San Andreas Fault. In *Fault Mechanics and Transport Properties of Rocks* (Vol. 51, pp. 475–503). San Diego, California: Elsevier. https://doi.org/10.1016/S0074-6142(08)62835-1

Rice, J. R. (1993). Spatio-temporal complexity of slip on a fault. *Journal of Geophysical Research*, *98*(B6), 9885. https://doi.org/10.1029/93JB00191

Rubin, A. M., & Ampuero, J.-P. (2005). Earthquake nucleation on (aging) rate and state faults: Rate and state earthquake nucleation. *Journal of Geophysical Research: Solid Earth*, *110*(B11). https://doi.org/10.1029/2005JB003686

Rushing, T. M., & Lay, T. (2012). Analysis of seismic magnitude differentials (m b−M w) across megathrust faults in the vicinity of recent great earthquakes. *Earth, Planets and Space*, *64*(12), 1199–1207. https://doi.org/10.5047/eps.2012.08.006

Sallarès, V., & Ranero, C. R. (2019). Upper-plate rigidity determines depth-varying rupture behaviour of megathrust earthquakes. *Nature*, *576*(7785), 96–101. https://doi.org/10.1038/s41586-019-1784-0

Sallarès, V., Prada, M., Riquelme, S., Meléndez, A., Calahorrano, A., Grevemeyer, I., & Ranero, C. R. (2021). Large slip, long duration, and moderate shaking of the Nicaragua 1992 tsunami earthquake caused by low near-trench rock rigidity. *Science Advances*, *7*(32), eabg8659. https://doi.org/10.1126/sciadv.abg8659

Scholz, C. H. (1998). Earthquakes and friction laws. *Nature*, *391*(6662), 37–42. https://doi.org/10.1038/34097

Tong, X., Sandwell, D., Luttrell, K., Brooks, B., Bevis, M., Shimada, M., et al. (2010). The 2010 Maule, Chile earthquake: Downdip rupture limit revealed by space geodesy. *Geophysical Research Letters*, *37*(24), L24311. https://doi.org/10.1029/2010GL045805

Ye, L., Lay, T., Kanamori, H., & Rivera, L. (2016). Rupture characteristics of major and great (M_w ≥ 7.0) megathrust earthquakes from 1990 to 2015: 2. Depth dependence. *Journal of*

Geophysical Research: Solid Earth, *121*(2), 845–863. https://doi.org/10.1002/2015JB012427